Linear Friction Welding of Dissimilar Materials 316L Stainless Steel to Zircaloy-4

P. WANJARA, B.S. NAIK, Q. YANG, X. CAO, J. GHOLIPOUR, and D.L. CHEN

In the nuclear industry, there are a number of applications where the transition of stainless steel to Zircaloy is of technological importance. However, due to the differences in their properties there are considerable challenges associated with developing a joining process that will sufficiently limit the heat input and welding time—so as to minimize the extent of interaction at the joint interface and the resulting formation of intermetallic compounds—but still render a functional metallurgical bond between these two alloys. As such, linear friction welding, a solid-state joining technology, was selected in the present study to assess the feasibility of welding 316L stainless steel to Zircaloy-4. The dissimilar alloy welds were examined to evaluate their microstructural characteristics, microhardness evolution across the joint interface, static tensile properties, and fatigue behavior. Microstructural observations revealed a central intermixed region and, on the Zircaloy-4 side, dynamically recrystallized and thermomechanically affected zones were present. By contrast, deformation on the 316L stainless steel side was limited. In the intermixed region a drastic change in the composition was observed along with a local increase in hardness, which was attributed to the presence of intermetallic compounds, such as $FeZr_3$ and Cr_2Zr. The average yield (316 MPa) and ultimate tensile (421 MPa) strengths met the minimum strength properties of Zircaloy-4, but the elongation was relatively low (~ 2 pct). The tensile and fatigue fracture of the welds always occurred at the interface in the mode of partial cohesive failure.

I. INTRODUCTION

ZIRCONIUM alloys, such as Zircaloy-4 (Zr-4), are candidate materials for various applications in nuclear fuel reprocessing plants requiring corrosion and irradiation resistance, low neutron absorption/capture cross section, and good mechanical properties at elevated temperatures.[1] However, a longstanding and unresolved issue for the application of these materials in the nuclear industry is their joining to stainless steels (SS), such as austenitic 316L SS, that is widely used as a structural material in nuclear reactors for its hot corrosion resistance, good strength, and durability.[2]

Over the years, different joining technologies have been studied to assemble a dissimilar joint between stainless steels and zirconium alloys. For instance, studies on diffusion bonding of stainless steels to Zircaloys have been shown to result in the formation of brittle intermetallic compounds within the interfacial diffusion zone due to the reaction of Zr with the diffused elements, including Ni, Fe, and Cr, from the stainless steel[3–7] and/or applied intermediate layers, such as Fe,[8] Ta,[9] Ti,[10] and multi-materials.[11,12] Studies on fusion welding, including gas tungsten arc welding and electron beam welding of stainless steel to Zr-4,[13–15] have revealed a high hardness fusion zone within which brittle intermetallic compounds and microfissures were present. By contrast, studies on rotary friction welding presented distinct advantages of limiting intermetallic compounds from forming during solid-state joining of stainless steel to Zircaloy[16,17] and the joints exhibited tensile strengths of ~ 420 MPa and up to 3 pct elongation during tensile loading at room temperature.[18]

A recent addition to the category of frictional joining technologies is linear friction welding (LFW), which enables assembly of a wider range of part geometries—such as rectangular and irregular cross sections—relative to rotary friction welding that is limited to round, symmetrical parts. As such, LFW is advantageous for joining complex assemblies consisting of multiple parts and a number of weld sites. Presently, LFW has been used successfully to join a wide range of titanium alloys,[19–22] polycrystalline,[23–30] and single

P. WANJARA, Q. YANG, X. CAO, and J. GHOLIPOUR are with the National Research Council Canada - Aerospace, 5145 Decelles Avenue, Montreal, Quebec H3T 2B2, Canada. Contact e-mail: priti.wanjara@cnrc-nrc.gc.ca B.S. NAIK and D.L. CHEN are with the Department of Mechanical and Industrial Engineering, Ryerson University, 350 Victoria Street, Toronto, Ontario M5B 2K3, Canada.

crystal[31,32] nickel-based superalloys, as well as dissimilar alloy combinations of aluminum to copper,[33,34] aluminum to magnesium,[35] and titanium to nickel-based superalloys.[36] However, the open literature presently contains no reported study on LFW of stainless steel to zirconium.[37] Hence, in the present study, the feasibility of manufacturing a dissimilar joint between 316L SS and Zr-4 was explored using the LFW process. The microstructural characteristics and microhardness evolution across the 316L SS/Zr-4 joints, as well as the tensile and fatigue properties of the assembly, were evaluated.

II. EXPERIMENTAL PROCEDURE

The as-received annealed 316L SS (UNS S31603) and Zr-4 (UNS R60804) base materials were received from ATI Specialty Alloys and Components (Albany, OR) in wrought form with a thickness of 35 mm and their chemical compositions are as given in Table I. Weld coupons of 12 mm width (W), 26 mm height (H), and 35 mm length (L) were obtained by electro-discharge machining (EDM) of the 316L SS and Zr-4 alloys. Just before placing the coupons in the welding fixture, the faying surfaces at the joint interface were lightly sanded using 320-grit sandpaper and cleaned with alcohol. It is noteworthy that select 316L SS coupons were pre-drilled with a 2-mm-diameter (ϕ) channel to allow the insertion of a K-type thermocouple for temperature measurement during LFW (Figure 1(a)). Specifically, the channel was drilled in the center of the coupon to permit the tip of the thermocouple to rest at a distance of 0.5 mm from the interface surface before LFW. Also, a Raytek Marathon infrared pyrometer, targeted at the interface, was used to measure the surface temperature during LFW at two locations (A and B) as indicated in Figure 1(a). To assure accuracy of the surface temperature measurements, the infrared pyrometer used in this study was blackbody calibrated to NIST traceability. However, having calibrated the infrared pyrometer on a blackbody source (or perfect radiator), the ability to measure the temperature on the interface of the 316L SS/Zr-4 assembly depends directly on the actual surface emissivity within the process temperature range. Hence, the methodology used to determine the average emissivity value involved heating the 316L SS/Zr-4 samples to six temperatures (600 °C, 700 °C, 800 °C, 900 °C, 1000 °C, and 1100 °C) that were measured with a contact thermocouple placed on the interface surface. Then for each target temperature, the surface temperature on the interface was measured also with the infrared pyrometer. The emissivity was adjusted until the surface temperature of the pyrometer corresponded to that of the contact thermocouple.

LFW entails oscillating one part under an applied pressure against another stationary part. Once frictional heating softens the interface, the reciprocating action stops and a forging force is applied to join the parts together. The equipment used for welding was an MTS LFW process development system (PDS) that comprised two hydraulic actuators: the in-plane actuator that

oscillates the lower part (316L SS) in the horizontal direction and the forge actuator that applies a downward load through the top stationary part (Zr-4). The LFW experiments were conducted in air (without shielding gas protection) at an ambient temperature of 25 °C. More details about the technical specifications of the MTS LFW PDS system are provided in Reference 38 and the process conditions used for LFW the 316L SS to the Zr-4 are given in Table II.

After LFW, the welds were sectioned transverse to the oscillation direction through the weld zone (as shown in Figure 1(b)) and prepared for metallographic examination using standard grinding and polishing techniques to obtain a finish of 0.04 micron. To examine the microstructures in the different regions of the 316L SS/Zr-4 welds, a sequential etching process was undertaken. First, the 316L SS side was masked with transparent tape, while the Zr-4 side was immersed in a solution of 5 mL HF, 10 mL HNO_3, and 100 mL glycerol $C_3H_8O_3$ and electrolytically etched at room temperature using an austenitic stainless steel cathode at 6 V for 30 to 60 seconds. Next, the transparent tape on the 316L SS side was removed, while the etched Zr-4 side was masked. The 316L SS side was then immersed in oxalic acid (10 g Oxalic, 100 mL H_2O) and electroetched at room temperature using an austenitic stainless steel cathode at 6 V for 30 to 60 seconds. Microstructural analysis to examine the various regions of the weld was carried out using an inverted optical microscope (Olympus GX71) equipped with digital image analysis software (AnalySIS Five) for the measurement of the grain size and phase fractions. High-resolution secondary electron (SE) imaging of the regions in the vicinity of the interface on the 316L SS and Zr-4 sides was undertaken using a Philips XL30S field emission gun (FEG) scanning electron microscope at 20 keV. The characteristics of the interface were examined on a polished surface using backscattered electron (BSE) imaging on a JSM-6380LV scanning electron microscope at 20 keV that was equipped with an Oxford energy dispersive X-ray spectroscopy (EDS) system for elemental composition analysis and line scanning. It is noteworthy that this latter system was equipped with three-dimensional (3D) fractographic analysis capacity, which supported compositional analysis on the fracture surfaces.

The microhardness profiles were measured across the welded samples (with a polished surface finish) at a load of 200 g and a dwell time of 15 seconds using a Struers Duramin A300 Vickers machine with a fully automated testing cycle (stage, load, focus, measure) that was calibrated using a standard reference test block prior to testing. For each weld condition, three hardness profiles across the weld were obtained with an indent interval of 0.2 mm (*i.e.*, at least three times the diagonal length of the indentation, so as to prevent any potential effect of strain fields caused by adjacent indentations).

The ASTM E8M-16a standard[39] served as a guideline for the tensile tests conducted in this work. Three tensile samples (Figure 1(b)) from three welds having a standard sub-sized geometry of 25 mm in gage length, 6 mm in width, and 3 mm in thickness (Figure 1(c)) were machined. All specimens were tested at room

Fig. 1—Schematic diagram showing (*a*) the 316L SS and Zr-4 coupons and the location of the temperature measurements with a thermocouple and pyrometer where WD is the welding direction (oscillatory movement) and RD is rolling direction, (*b*) the linear friction-welded coupons used to extract the tensile, metallography, and fatigue samples, and (*c*) the geometry of the tensile and fatigue samples.

temperature using a 250 kN MTS 810 tensile machine equipped with a laser extensometer. Tensile tests were conducted until failure using displacement control at a crosshead speed of 2 mm/min. The tensile properties evaluated in this work included the yield strength (YS), ultimate tensile strength (UTS), and percent elongation (percent El).

The ASTM E466-15 standard[40] served as a guideline for conducting load-controlled constant amplitude axial fatigue testing of the welds. Specifically, 13 linear friction welds were manufactured and two fatigue samples were extracted from each weld for fatigue testing (Figure 1(b)). The fatigue samples had a geometry as specified in Figure 1(c) and a ground surface finish specified with a maximum roughness (R_a) of 0.4 μm. Before fatigue testing, all the lateral edges of the fatigue samples were lightly ground using successively finer sandpapers from 320-grit ($R_a \sim 0.3$ μm) to 600-grit ($R_a \sim 0.1$ μm) in order to avoid the influence of local surface stress concentration. Fatigue tests were performed using a fully computerized Instron 8801 servo-hydraulic testing system under load control. Sinusoidal loading with a frequency of 50 Hz and a load ratio R (= P_{min}/P_{max}) of 0.2 was applied in the fatigue tests. The stress was calculated as the applied load divided by the sample cross-sectional area. At least two samples were tested at each cyclic load level. All mechanical tests were performed up to failure. The fracture surface of the 316L SS/Zr-4 linear friction welds after fatigue testing was examined using scanning electron microscopy (SEM). Also, X-ray diffraction (XRD) analysis was undertaken on the fracture surface of the fatigued samples to characterize the intermixed zone between 316L SS and Zr-4. Specifically XRD patterns were obtained using Cu K$_\alpha$ radiation at 45 kV and 40 mA. The diffraction angle (2θ) at which the X-rays encroached on the sample varied from 20 to 90 deg with a step size of 0.05 deg and 3 seconds in each step.

III. RESULTS AND DISCUSSION

A. *Thermal Analysis*

During LFW, the temperatures measured by means of the thermocouple embedded inside the 316L SS coupon permitted examination of the thermal evolution at the weld center roughly 0.5 mm from the interface. By contrast, using a pyrometer, the temperature evolution on the surface at the interface was measured at locations
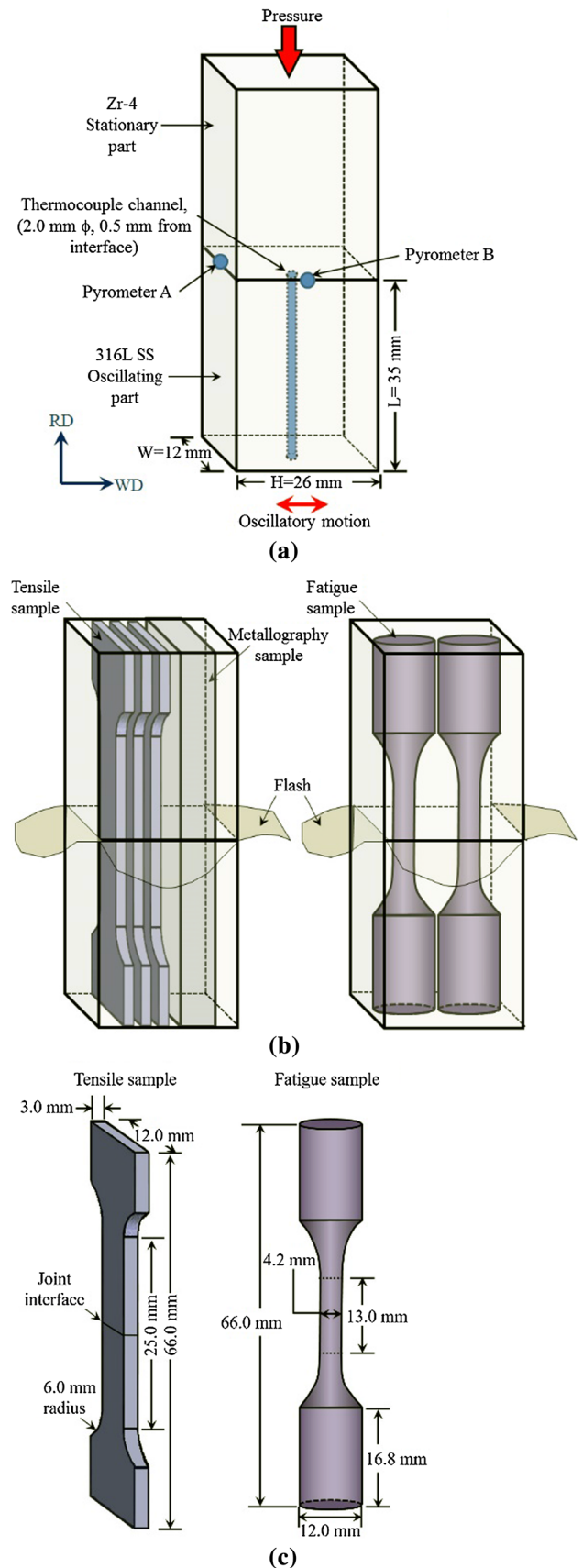
Table I. Chemical Composition of the 316L SS and Zr-4 (wt pct)

Materials	Zr	Fe	Cr	Ni	Mo	Mn	Si	P	S	C	Sn	O
316 L SS (UNS S31603)	—	65	17	12	2.50	2	1	0.045	0.03	0.03	—	—
Zr-4 (UNS R60804)	98	0.22	0.12	—	—	—	—	—	—	—	1.57	0.15

Table II. Process Parameters Used for the Linear Friction Welding of 316L SS to Zr-4

	Conditioning Phase	Burn Off Phase	Forging Phase
Pressure (MPa)	70	100	150
Frequency (Hz)	100	100	—
Amplitude (mm)	± 2	± 2	—
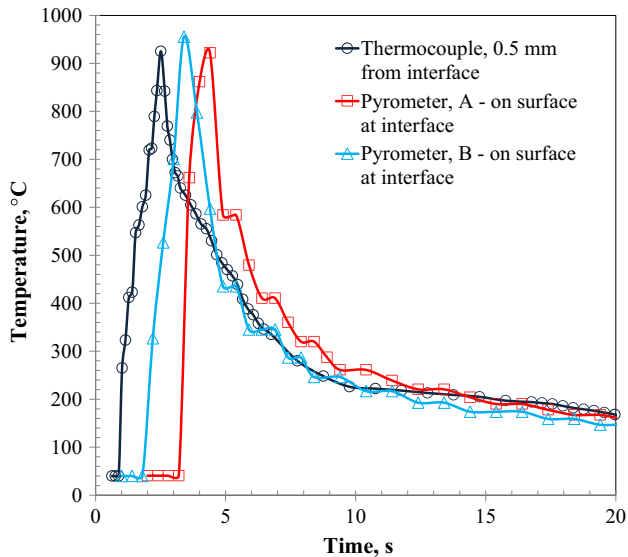
Fig. 2—Thermal profiles measured during LFW of 316L SS to Zr-4, where the start time of the individual curves has been staggered to facilitate visualization of the peak values.
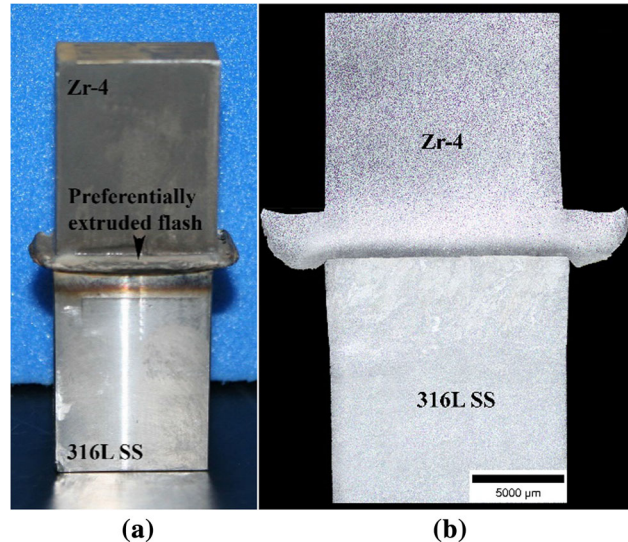

Fig. 3—The 316L SS/Zr-4 linear friction weld showing the preferentially extruded flash that forms almost entirely from the Zr-4 half of weld (a) as-welded joint and (b) optical micrograph of transverse cross section cut parallel to the welding direction.

A and B, as indicated in Figure 1(a). From the thermal analysis curves shown in Figure 2, the maximum temperatures measured on the surface at the interface ranged between 922 °C and 956 °C, while at the weld center (0.5 mm from the interface) a peak value of 925 °C was recorded in the 316L SS. Overall there is good agreement between the three thermal profiles, though the measurement with the thermocouple faced some challenges due to the oscillatory motion. Also, the present results corroborate well with previous data from rotary frictional welding of EN 58B SS (equivalent to type 321 SS) to Zircaloy-2 (Zr-2) that indicated a peak temperature of 935 °C for the weld center at 0.1 mm from the interface.[18]

B. Inspection

Visual examination of the dissimilar alloy welds revealed that the flash layer originated mainly from expulsion of the Zr-4 with limited deformation of the 316L SS (Figures 3(a) and 3(b)) and is consistent with the preferential extrusion reported for LFW of dissimilar materials, such as Al-Cu,[33] Al-Mg,[35] and Ti-Ni.[36] Also, previous findings on friction welding of 304L SS to Zr-4 reported that only the latter alloy underwent deformation and contributed to the formation of the flash layer in the assembly.[17] In addition, Kilbride and Adams[18] reported that even when the stainless steel is preheated to 800 °C before friction welding, flash formation occurs exclusively from Zr-2.

Non-destructive inspection of the as-welded joints showed no indications using radiographic, ultrasonic, and liquid penetrant testing in accordance with ASME BPVC-III-2017.[41] To confirm that the lack of indications was actually related to the absence of discontinuities/defects in the welds, metallographic examination was also undertaken. As illustrated in Figure 3(b) for a transverse cross section parallel to the welding/oscillation direction, examination of the joint area across the weld revealed intimate contact between the 316L SS and Zr-4 at the interface and integral bonding without the presence of discontinuities, such as residual oxides, pores, or cracks.
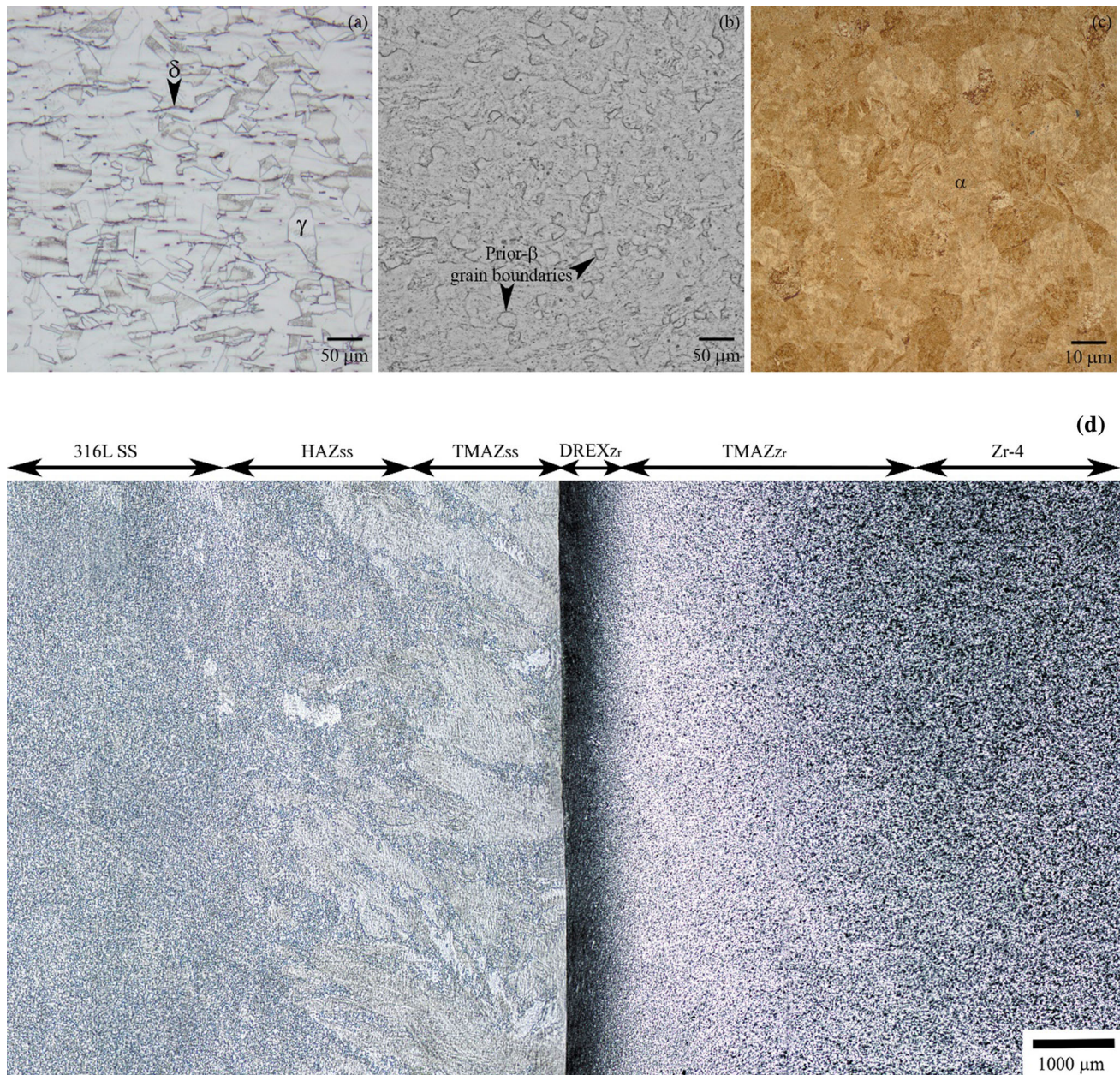
Fig. 4—Typical microstructures of (a) 316L SS base metal, (b, c) Zr-4 base metal, and (d) 316L SS/Zr-4 linear friction weld (transverse cross section cut perpendicular to the welding direction).

C. Microstructure

The as-received 316L SS microstructure consisted of a polyhedral grain structure of austenite (γ) with 3.4 ± 0.3 pct of delta ferrite (δ) present as stringers oriented along the rolling direction, as shown in Figure 4(a). The average size of the austenite grains was 47 ± 9 μm measured by the linear intercept method described in Reference 42. By contrast, the Zr-4 as-received microstructure consisted of finely equiaxed prior-beta grains with an average size of 21 ± 5 μm. Within these prior-beta grains, a typical basketweave

structure of alpha (α) phase plates was observed (Figures 4(b) and 4(c)).

Detailed examinations of the joint area revealed a thermomechanically affected zone (TMAZ) and heat-affected zone (HAZ) on the 316L SS side, as well as a dynamically recrystallized zone (DREX) and TMAZ on the Zr-4 side, as shown in Figure 4(d). In particular, from a distance of roughly 5 mm from the interface on the 316L SS side and Zr-4 side, the etching response was seen to be affected. However, it was difficult to statistically quantify microstructural changes in HAZ_{SS} that

may have resulted from, for instance, growth of the austenitic grains. Similarly, in the TMAZ$_{Zr}$ changes in the alpha grain structure due to, for instance, strain hardening and/or alpha → alpha + beta phase transformation that starts at ~ 810 °C[43] were not differentiable relative to the base material microstructure. However, within TMAZ$_{SS}$, especially in the vicinity of the interface, deformation bands in the 316L SS could be discerned at high resolution using FEG-SEM, as illustrated in Figure 5(a). The limited deformation in TMAZ$_{SS}$ is reasonable considering that, at the peak temperatures recorded during LFW (956 °C), 316L SS retains considerable high-temperature strength and resistance to deformation.[18,44] By contrast, in DREX$_{Zr}$, the equiaxed prior-beta grain structure of the Zr-4 base material underwent significant plastic deformation at elevated temperatures and a fine recrystallized microstructure was apparent, as revealed in Figure 5(b), especially just adjacent to the interface. The occurrence of dynamic recrystallization in DREX$_{Zr}$ during LFW may be reasoned on the premise of the severe deformation of Zr-4 at high strain rates and elevated temperatures. In LFW, the maximum deformation in the material depends on the distance traveled from the opposite extreme points of oscillation. This deformation occurs in half a cycle, so the strain rate can be estimated using an average velocity—amplitude (a) × frequency (f)—over the total length (l) traveled[45,46]:

$$\dot{\varepsilon} = \frac{af}{l} \quad [1]$$

The average strain concentrated at the interface can then be estimated using the measured welding time (~ 3 seconds) in conjunction with the average strain rate. Thus, for the LFW conditions applied in the present work to join Zr-4 and 316L SS, the average strain rate locally at the interface would be ~ 7.7 s^{-1} with an average strain of 23 and temperatures in the vicinity of the beta transus (~ 980 °C).

Previously, Liss et al.[47] followed the thermo-mechanical response of Zr-4 through in situ X-ray diffraction observations and concluded that the low-temperature alpha phase gradually transforms to the high-temperature beta phase upon heating without significant grain growth; this explains the difficulty encountered in the present work to differentiate microstructural changes in TMAZ$_{Zr}$. For deformation at relatively low temperatures (500 °C) in the alpha-beta region, Chauvy et al.[48] reported that strain hardening occurs before flow softening in Zr-4. With increasing temperature approaching the beta transus, the flow stress of Zr-4 rapidly decreases[48] and plastic deformation accelerates,[46] which in turn results in regimes of dynamic recovery and dynamic recrystallization.[48] Indeed, Logé et al.[49] reported the occurrence of dynamic recrystallization in Zr-4 during hot deformation at temperatures above 750 °C at strain rates of 0.1 and 1 s^{-1}. In view of these previous findings, the above analysis of the prevalent deformation conditions (strain rate, temperature, and strain) indicates that restoration processes such as dynamic recrystallization are operative locally in DREX$_{Zr}$ during LFW of 316L SS to Zr-4.

D. Weld Interface

To observe the characteristics of the weld interface between the 316L SS and Zr-4 at high resolution, BSE imaging was carried out using SEM, as illustrated in Figure 6. In particular, the interface between 316L SS and Zr-4 comprised a continuous intermixed region with a fairly uniform thickness of 3 μm. This finding agrees well with the ~ 4-μm-thick interface observed for friction-welded 304L SS to Zr-4 in Reference 17.

To characterize the distribution of elements in the intermixed region at the interface, SEM-EDS line scans from the 316L SS to Zr-4 were undertaken for all major elements present in both alloys, including zirconium (Zr), iron (Fe), and chromium (Cr), as illustrated in Figure 7 that corresponds to the path identified in Figure 6. There is a diffusion profile for each element in the intermixed region. For friction welding of EN 58B SS (equivalent to type 321 SS) to Zr-2, Kilbride et al.[18] identified similar diffusion plateaus for Fe, Cr, Ni, and Zr across a 35-μm-thick interface using electron microprobe analysis, which overall agrees well with the findings in the present work with exception of the absence of Ni. It is noteworthy that Zr-4 was designed for a reduced tendency of hydrogen pickup by limiting the iron (0.12 to 0.18 pct) and nickel (0.007 pct maximum) contents in the compositional specification relative to Zr-2.[50] Hence, the temperature-dependent data on the diffusion of Ni, Cr, and Fe in Zr-2 generated systematically by Pande et al.[51,52] were deliberated for the present analysis. In particular, at the interface temperatures during LFW, Pande et al.[51,52] reported that the diffusion rate of Ni, Cr, and Fe in the beta phase of Zr-2 at 900 °C is 5.62 × 10^{-12} cm^2/s, 1.259 × 10^{-11} cm^2/s, and 1.318 × 10^{-11} cm^2/s, respectively, and the self-diffusion of Zr is ~ 1 × 10^{-9} cm^2/s.[53] The order of magnitude difference in the diffusivity of Ni relative to Cr and Fe as well as the short welding times and limited thickness (~3 μm) of the interface in the present work may reasonably account for the absence of Ni in the interface of 316L SS/Zr-4 linear friction welds.

E. Microhardness

Figure 8 shows the evolution in the microhardness across the interface of the 316L SS/Zr-4 linear friction weld. In particular, on the 316L SS side, though the etching response was affected in HAZ$_{SS}$, the hardness across this region was not noticeably different from that of the as-received 316L SS within the experimental error, which had an average hardness of 162 ± 3 HV. The hardness then increased gradually across TMAZ$_{SS}$, reaching an average value of 193 ± 4 HV—roughly 20 pct harder than the as-received 316L SS—just adjacent to the intermixed region at the interface. This local increase in hardness observed in TMAZ$_{SS}$ may be attributed to work hardening, as evidenced by the
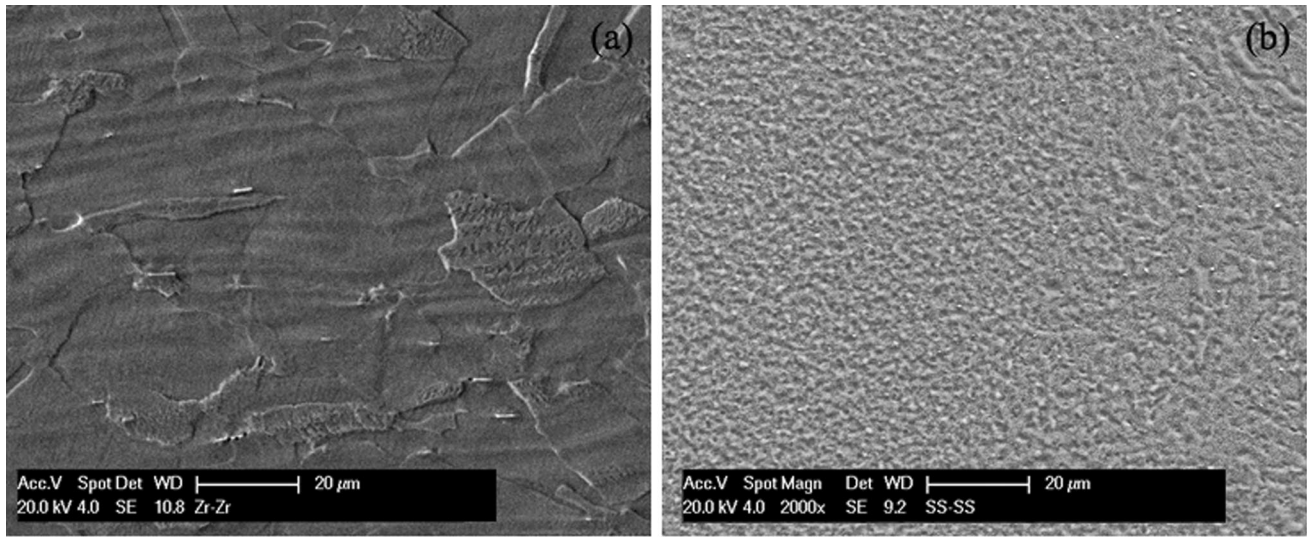
Fig. 5—FEG-SEM images of (*a*) the deformation bands (wavy lines) in TMAZ$_{SS}$ on the 316L SS side and (*b*) the recrystallized fine grains in DREX$_{Zr}$ on the Zr-4 side of the dissimilar alloy weld.
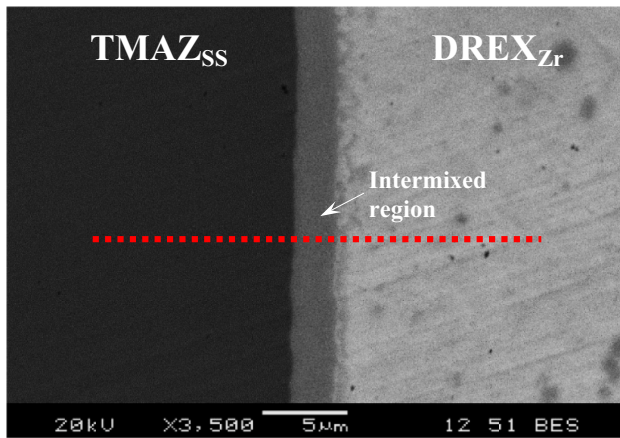

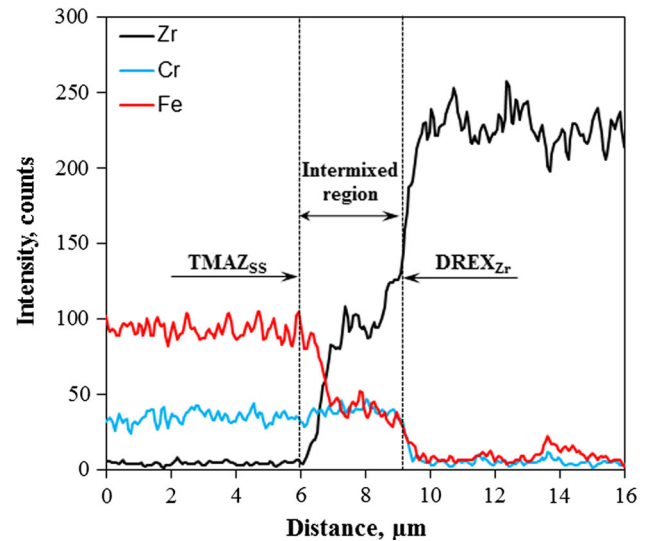Fig. 6—BSE-SEM image of the intermixed region at the joint interface in the 316L SS/Zr-4 linear friction weld.

Fig. 7—SEM-EDS elemental line scans from the 316L SS side on the left, across the intermixed region at the interface, and to the Zr-4 side on the right (corresponding to red line demarcated in Fig. 6) (Color figure online).

deformed microstructure of the 316L SS in the vicinity of the interface (Figure 5(a)). The Zr-4 side exhibited an increase of 8 pct in the hardness that occurred progressively across the TMAZ$_{Zr}$ and DREX$_{Zr}$ regions, from the average value of 185 ± 3 HV in the as-received Zr-4 to 200 ± 4 HV just adjacent to the intermixed region at the interface. In DREX$_{Zr}$ region, this hardness increase is likely attributable to the refined grain structure of the alpha matrix that results from the occurrence of dynamic recrystallization during LFW. By contrast, at lower temperatures and strain rates in TMAZ$_{Zr}$, the increase in hardness may be attributed to strain hardening and/or the reverse alpha ⇌ alpha + beta phase transformation. At the interface between the 316L SS and Zr-4, the average hardness measured locally in the intermixed region was 250 ± 9 HV. These findings for the 316L SS/Zr-4 linear friction weld are consistent with the previous observations reported for friction welding of 304L SS to Zr-4; specifically, the hardness increases in the vicinity of the interface on the 304L SS and Zr-4

sides were attributed to strain hardening in the former and a recrystallized structure in the latter.[17]

F. Tensile Properties

The static tensile properties measured for the 316L SS/Zr-4 linear friction welds, listed in Table III, indicated average values for the yield strength (YS), ultimate tensile strength (UTS), elastic modulus (E), and percent elongation (percent El) of 316 ± 9 MPa, 418 ± 14 MPa, 147 ± 10 GPa, and 2.1 ± 0.1 pct, respectively, with failure occurring at the interface (in the intermixed region). Previously, Kilbridge et al.[18] reported maximum fracture stresses of 203 to 218 MPa with an elongation of 2 to 4 pct for a friction-welded EN 58B (321) SS/Zr-2 joint.[18]
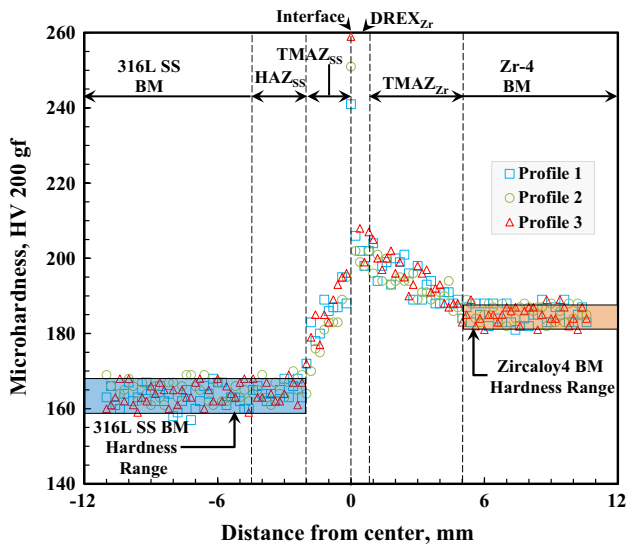
Fig. 8—Typical microhardness profile measured for the 316L SS/Zr-4 linear friction weld.

More recently, for 304L SS/Zr-4 friction welds, Shankar et al.[17] reported a relatively high maximum fracture stress (540 MPa)—but not the associated elongation—and found that the bend ductility was limited with fracture occurring at the interface at a 5 deg bend angle. In the present work, the LFW conditions applied to assemble 316L SS to Zr-4 gave relatively high values for the YS and UTS (or fracture stress)—that met the minimum tensile strength properties specified for Zr-4[55]—and permitted some retention of ductility.

G. Fatigue Properties

Fatigue tests were performed to evaluate the strength of the 316L SS/Zr-4 linear friction welds under cyclic loading at room temperature (RT), $R = 0.2$ and 50 Hz. The fatigue experimental data for the 316L SS/Zr-4 welds are plotted in Figure 9(a) in the form of the maximum stress as a function of number of cycles to failure (N_f), and in Figure 9(b) in a double log scale of the maximum stress vs the number of reversals to failure ($2N_f$). Low-cycle fatigue (LCF) properties of the 316L
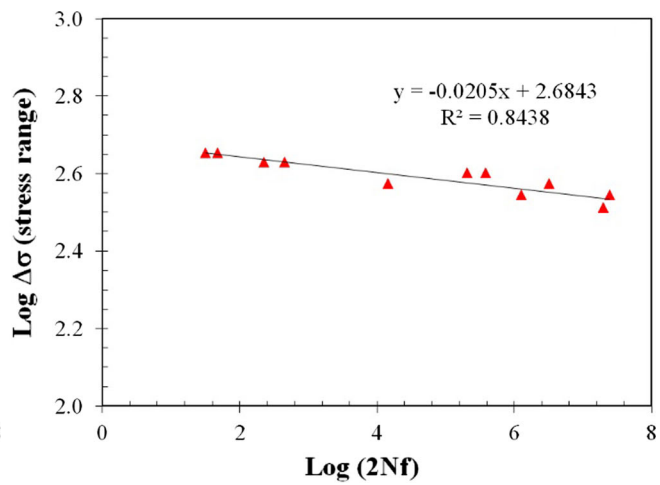
Table III. Tensile Mechanical Properties of 316L SS/Zr-4 Linear Friction Welds

Sample	YS (MPa)	UTS** (MPa)	E (GPa)	Percent El (Pct)	Failure Location
316L SS* [54]	235	560	193	55	N/A
Zr-4* [55]	241	413	99.3	20	
316L SS/Zr-4	308	420	150	2.1	interface
	314	404	136	1.9	
	326	432	156	2.2	
Average	316 ± 9	418 ± 14	147 ± 10	2.1 ± 0.1	

*Specified minimum values.
**Fracture stress.
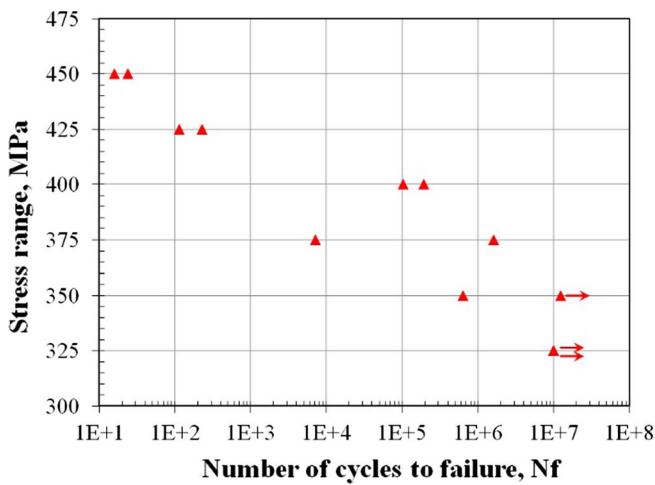
(a)

(b)

Fig. 9—Fatigue life curves of the 316L SS/Zr-4 linear friction welds tested at room temperature, $R = 0.2$ and 50 Hz: (a) semi-log scale plot of the maximum stress versus the number of cycles to failure (N_f) and (b) double log scale plot of the maximum stress versus the number of reversals to failure ($2N_f$).
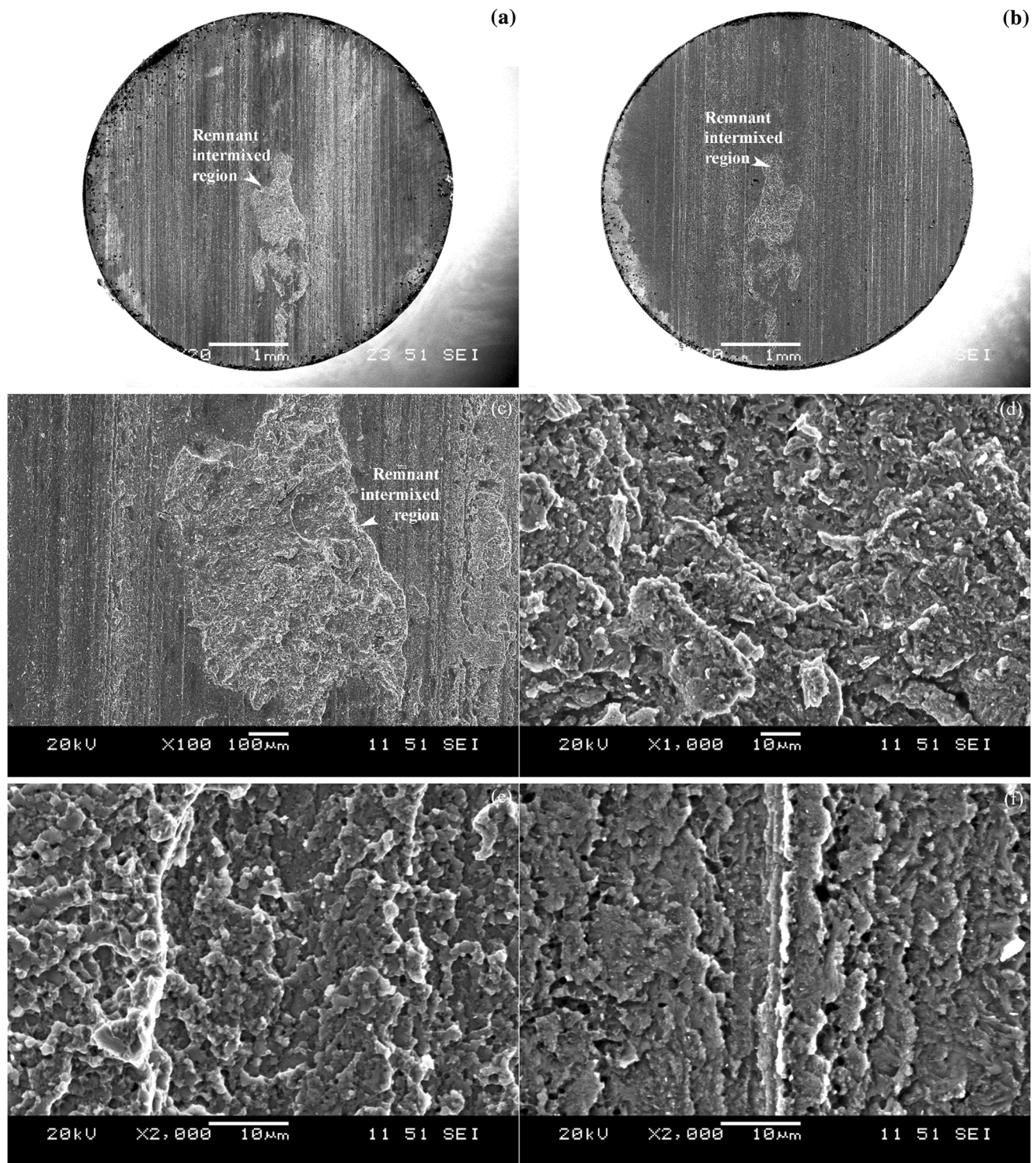
Fig. 10—Typical SEM images of the fatigue fracture surface of 316L SS/Zr-4 linear friction welds: (*a*) overall fatigue fracture surface on the 316L SS side, (*b*) overall fatigue fracture surface on the Zr-4 side, (*c*) intermixed region on 316L SS side at higher magnification, (*d*) intermixed region at higher magnification on Zr-4 side, and (*e*, *f*) crack propagation region at a further higher magnification.

SS/Zr-4 welds have industrial relevance for nuclear applications where power fluctuations within the reactor give rise to thermal expansion and contraction of the materials that result in plastic straining. The LCF behavior of the 316L SS/Zr-4 linear friction welds is characterized by relatively high maximum stress values (~ 425 to 450 MPa) that lend good assurance of the weld integrity. Also, in the high-cycle fatigue (HCF) region, a fatigue limit as characterized by the maximum stress value of 325 MPa at 10^7 cycles was achieved for
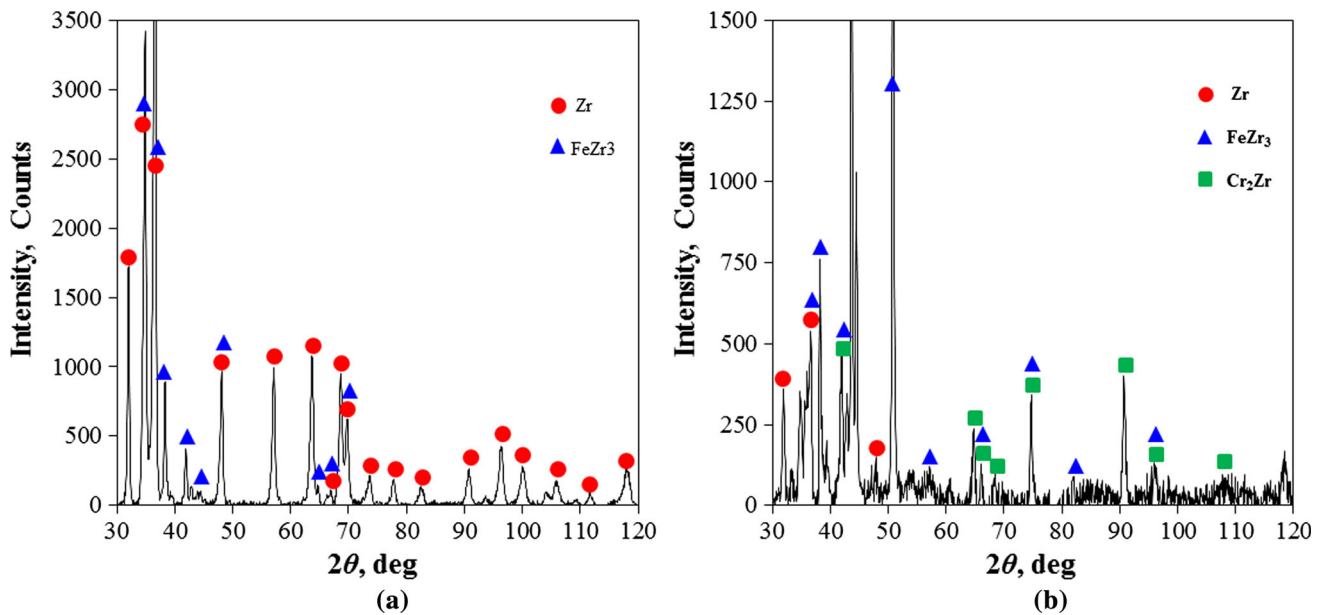
Fig. 11—Typical XRD profiles obtained on the fracture surfaces of the fatigue tested 316L SS/Zr-4 linear friction welds (*a*) 316L SS side and (*b*) Zr-4 side.

the 316L SS/Zr-4 welds. Given the absence of fatigue data for 316L SS/Zr-4 joints in the open literature, an instructive comparison to the limited information on the LCF behavior of Zr-4[56] was undertaken. Specifically, at a maximum stress of 400 MPa, LCF failure of Zr-4 at room temperature ($R = 0.1$ and 60 to 65 Hz) was reported at 4.4×10^5 and 3.6×10^5 cycles in the rolling and transverse directions.[56] Hence the 316L SS/Zr-4 linear friction welds, that exhibited experimentally roughly 10^5 cycles at a maximum stress value of 400 MPa, as indicated in Figure 9(a), are relatively close to the fatigue strength of Zr-4. It is noteworthy, however, that the fatigue data for the 316L SS/Zr-4 linear friction welds exhibited some extent of experimental scatter, which was wider in the HCF regime relative to the LCF. This finding is consistent with previous results[57] from cyclic pressurization of Zr-4 that illustrated a stress-life diagram with increased data scatter above 10^3 cycles.

H. *XRD Analysis on the Fracture Surfaces*

Fracture of 316L SS/Zr-4 linear friction welds during fatigue testing occurred mainly at the joint interface, but the fracture surface exhibited remnant areas of the intermixed region on both the 316L SS and Zr-4 sides, as shown in Figures 10(a) and 10(b), with magnified images shown in Figures 10(c) and 10(d). This indicated a mode of partial "cohesive" failure during fatigue testing. A similar cohesive failure mode has also been observed in other welded dissimilar joints, *e.g.*, magnesium-to-aluminum alloy joints and copper-to-magnesium alloy joints.[58–61] In the absence of appreciable plastic deformation (as noted during tensile loading), rapid crack propagation that continued through the intermixed region is apparent in Figures 10(e) and 10(f). The nature of the phases present in the intermixed

region was investigated by XRD analysis on the fatigue fracture surfaces of both sides. Figures 11(a) and 11(b) show the results of the XRD analysis undertaken on the 316L SS and Zr-4 sides of a fatigue-fractured sample. The XRD analysis revealed distinct peaks of the $FeZr_3$ and Cr_2Zr intermetallic phases, along with some peaks that overlapped with the Zr-4 base material spectrum. These results agree well with the elemental results from the SEM-EDS line scans (Figure 7). From the Fe-Zr phase diagram,[62] at the temperatures experienced during LFW, the high-temperature $FeZr_2$, which is stable between 780 and 951 °C may have formed initially and then $FeZr_3$ may have formed peritectically from the phases $FeZr_2$ and beta-Zr at 851 °C, as shown on both the 316L SS and Zr-4 sides in Figure 11. This corroborates the cohesive failure mode, as mentioned above. The Cr_2Zr Laves phase in Zr-Cr phase diagram[63] exhibits polymorphism and can crystallize as different ordered polytypes,[64] including (1) hexagonal C14 that is stable between 1640 °C and 1673 °C, (2) hexagonal C36 that is stable between 1573 and 1640 °C, and (3) cubic C15 phase below 1573 °C. These findings of intermetallic phases in the intermixed region between 316L SS and Zr-4 agree generally well with findings for 304L SS/Zr-4 assemblies that reported a host of different phases such as $Zr(Cr,Fe)_2$, $ZrCr_2$, Zr_2Fe-Zr_2Ni, $Ni_{11}Zr_9$, and Ni_7Zr_2 during fusion welding,[14,15] diffusion bonding,[4] and friction welding.[17]

IV. CONCLUSIONS

In the present study, the feasibility of applying the linear friction welding (LFW) process to join dissimilar alloys 316L stainless steel (SS) and Zircaloy-4 (Zr-4) was assessed. The following conclusions can be drawn based

on the observations of the microstructural characteristics, as well as analyses of the thermal data, microhardness evolution, tensile and fatigue properties, and X-ray diffraction (XRD) data:

1. Solid-state joining of 316L SS to Zr-4 is feasible using the LFW technology and peak temperatures between 922 and 956 °C were observed at the interface on the surface. During LFW, Zr-4 preferentially extrudes at the interface and forms a single flash layer.
2. The interface between the 316L SS and Zr-4 exhibited intimate bonding without the presence of discontinuities, such as pores or cracks, and consisted of a continuous intermixed region having a uniform thickness of ~ 3 μm. The presence of Fe, Cr, and Zr in this intermixed region was ascertained using energy dispersive spectroscopy.
3. Examination of the microstructural evolution indicated extensive deformation near the interface on the Zr-4 side with the presence of a dynamically recrystallized zone (DREX) and a thermomechanically affected zone (TMAZ). By contrast, adjacent to interface on the 316L side, the deformation was limited but some deformation bands were observed in the TMAZ.
4. Microhardness measurements across the 316L SS/Zr-4 joints indicated that the hardness increased from a value of 162 ± 3 HV in 316L SS to 193 ± 4 HV just adjacent to the intermixed region at the joint interface. This hardness increase of 20 pct was attributed to the effect of work hardening in the TMAZ of 316L SS. By contrast, the hardness on the Zr-4 side exhibited an increase of 8 pct—from 185 ± 3 HV in the base material to 200 ± 4 HV just adjacent to the joint interface—which was attributed to the refined grain structure in the DREX and strain hardening in the TMAZ. At the joint interface (where the intermixed region was present), a peak local hardness of 250 ± 9 HV was obtained.
5. The 316L SS/Zr-4 linear friction welds exhibited good static tensile properties—with a yield strength of 316 ± 9 MPa, ultimate tensile strength of 418 ± 14 MPa, elastic modulus of 147 ± 10 GPa, and percent elongation of 2.1 ± 0.1 pct—and superior fatigue resistance with a fatigue limit of 325 MPa as characterized by the maximum stresses. Fatigue failure occurred exclusively at the interface.
6. XRD analysis of the intermixed region indicated the presence of Cr_2Zr and $FeZr_3$ intermetallic phases on the fatigue fracture surfaces of the 316L SS/Zr-4 linear friction welds. In particular, $FeZr_3$ intermetallic compound was present on both 316L SS and Zr-4 sides, corroborating the partial cohesive failure mode.

REFERENCES

1. E. Gutsmiedl and A. Scheuer: *Phys. B Condens. Matter*, 2002, vol. 311, pp. 182–90.
2. F. Cattant, D. Crusset, and D. Féron: *Mater. Today*, 2008, vol. 11, pp. 32–37.
3. G. Perona, R. Sesini, W. Nicodemi, and R. Zoja: *J. Nucl. Mater.*, 1966, vol. 18, pp. 278–91.
4. H.I. Shaaban, F.H. Hammad, and J.L. Baron: *J. Nucl. Mater.*, 1978, vol. 71, pp. 277–85.
5. P. Gr, I.Pătru. Lucuta, and F. Vasiliu: *J. Nucl. Mater.*, 1981, vol. 99, pp. 154–64.
6. M. Taouinet, S. Lebaili, and N. Souami: *Phys. Procedia*, 2009, vol. 2, pp. 1231–39.
7. A.A. Abou-Zahra and F.H. Hammad: *Materialwiss. Werkstofftech.*, 1979, vol. 10, pp. 349–53.
8. H.I. Shaaban, F.H. Hammad, and J.L. Baron: *J. Nucl. Mater.*, 1978, vol. 78, pp. 431–33.
9. M. Ahmad, J.I. Akhter, Q. Zaman, M.A. Shaikh, M. Akhtar, M. Iqbal, and E. Ahmed: *J. Nucl. Mater.*, 2003, vol. 317, pp. 212–16.
10. J.I. Akhter, M. Ahmad, M. Iqbal, M. Akhtar, and M.A. Shaikh: *J. Alloys Compd.*, 2005, vol. 399, pp. 96–100.
11. K. Bhanumurthy, J. Krishnan, G.B. Kale, R.K. Fotedar, A.R. Biswas, and R.N. Arya: *J. Mater. Process. Technol.*, 1995, vol. 54, pp. 322–25.
12. A. Munis, M. Ahmed, J.I. Akhter, G. Ali, and N.H. Tariq: *Proceedings of the 10th International Symposium on Advanced Materials*, Rawalpindi, Pakistan, 2007, pp. 157–59.
13. D. Mukherjee and J.P. Panakkal: *J. Mater. Sci. Lett.*, 1995, vol. 14, pp. 1383–85.
14. M. Ahmad, J.I. Akhter, M. Akhtar, and M. Iqbal: *J. Mater. Sci.*, 2007, vol. 42, pp. 328–31.
15. M. Ahmad, J.I. Akhter, M.A. Shaikh, M. Akhtar, M. Iqbal, and M.A. Chaudhry: *J. Nucl. Mater.*, 2002, vol. 301, pp. 118–21.
16. T.H. Hazlett: *Weld. J.*, 1962, vol. 41, pp. 448s–50s.
17. A.R. Shankar, S.S. Babu, M. Ashfaq, U.K. Mudali, K.P. Rao, N. Saibaba, and B. Raj: *J. Mater. Eng. Perform.*, 2009, vol. 18, pp. 1272–79.
18. J. Kilbride and D.F. Adams: *Weld. Metal Fabr.*, 1971, vol. 39, pp. 26–35.
19. J.C. Stinville, F. Bridier, D. Ponsen, P. Wanjara, and P. Bocher: *Int. J. Fatigue*, 2015, vol. 70, pp. 278–88.
20. P. Wanjara, E. Dalgaard, J. Gholipour, X. Cao, J. Cuddy, and J.J. Jonas: *Metall. Mater. Trans. A*, 2014, vol. 45A, pp. 5138–57.
21. E. Dalgaard, P. Wanjara, J. Gholipour, and J.J. Jonas: *Can. Metall. Q.*, 2012, vol. 51, pp. 269–76.
22. E. Dalgaard, P. Wanjara, J. Gholipour, X. Cao, and J.J. Jonas: *Acta Mater.*, 2012, vol. 60, pp. 770–80.
23. M. Smith, L. Bichler, J. Gholipour, and P. Wanjara: *Int. J. Adv. Manuf. Technol.*, 2017, vol. 90, pp. 1931–46.
24. A. Chamanfar, M. Jahazi, J. Gholipour, P. Wanjara, and S. Yue: *Mater. Charact.*, 2015, vol. 104, pp. 149–61.
25. A. Chamanfar, M. Jahazi, J. Gholipour, P. Wanjara, and S. Yue: *Metall. Mater. Trans. A*, 2013, vol. 44A, pp. 4230–38.
26. O.T. Ola, O.A. Ojo, P. Wanjara, and M.C. Chaturvedi: *Adv. Mater. Res.*, 2011, vol. 278, pp. 446–53.
27. A. Chamanfar, M. Jahazi, J. Gholipour, P. Wanjara, and S. Yue: *Mater. Sci. Eng. A*, 2012, vol. 555, pp. 117–30.
28. K.R. Vishwakarma, O.A. Ojo, P. Wanjara, and M.C. Chaturvedi: *JOM*, 2014, vol. 66, pp. 2525–34.
29. O.T. Ola, O.A. Ojo, P. Wanjara, and M.C. Chaturvedi: *Metall. Mater. Trans. A*, 2011, vol. 42A, pp. 3761–77.

30. A. Chamanfar, M. Jahazi, J. Gholipour, P. Wanjara, and S. Yue: *Mater. Des.*, 2012, vol. 36, pp. 113–22.
31. O.T. Ola, O.A. Ojo, P. Wanjara, and M.C. Chaturvedi: *Metall. Mater. Trans. A*, 2012, vol. 43A, pp. 921–33.
32. P. Wanjara, E. Dalgaard, J. Gholipour, and J. Larose: *Mater. Sci. Forum*, 2012, vols. 706–709, pp. 3022–27.
33. P. Wanjara, E. Dalgaard, G. Trigo, C. Mandache, G. Comeau, and J.J. Jonas: *Can. Metall. Q.*, 2011, vol. 50, pp. 350–59.
34. E. Dalgaard, P. Wanjara, G. Trigo, M. Jahazi, G. Comeau, and J.J. Jonas: *Can. Metall. Q.*, 2011, vol. 50, pp. 360–70.
35. I. Bhamji, M. Preuss, R.J. Moat, P.L. Threadgill, and A.C. Addison: *Sci. Technol. Weld. Joining*, 2012, vol. 17, pp. 368–74.
36. P. Wanjara, J. Gholipour, K. Watanabe, K. Nezaki, Y. Tian, and M. Brochu: *Mater. Sci. Forum*, 2017, vol. 879, pp. 2072–77.
37. W. Li, A. Vairis, M. Preuss, and T. Ma: *Int. Mater. Rev.*, 2016, vol. 61, pp. 71–100.
38. P. Wanjara and M. Jahazi: *Metall. Mater. Trans. A*, 2005, vol. 36A, pp. 2149–64.
39. ASTM E8M-16a, Standard test methods for tension testing of metallic materials (Metric).
40. ASTM E466-15: Standard practice for conducting force controlled constant amplitude axial fatigue tests of metallic materials.
41. ASME BPVC-III-2017: ASME boiler & pressure vessel code—section iii—rules for construction of nuclear power plant components.
42. ASTM E112-13: Standard test methods for determining average grain size.
43. H.M. Chung and T.F. Kassner: *J. Nucl. Mater.*, 1979, vol. 84, pp. 327–39.
44. R.K. Desu, H.N. Krishnamurthy, A. Balu, A.K. Gupta, and S.K. Singh: *J. Mater. Res. Technol.*, 2016, vol. 5, pp. 13–20.
45. A. Vairis and M. Frost: *Wear (Switzerland)*, 1998, vol. 217, pp. 117–31.
46. E. Dalgaard, F. Coghe, L. Rabet, M. Jahazi, P. Wanjara, and J.J. Jonas: *Adv. Mater. Res.*, 2010, vols. 89–91, pp. 124–29.
47. K.-D. Liss, U. Garbe, H. Li, T. Schambron, J.D. Almer, and K. Yan: *Adv. Eng. Mater.*, 2009, vol. 11, pp. 637–40.
48. C. Chauvy, P. Barbéris, and F. Montheillet: *Mater. Sci. Forum*, 2004, vols. 467–470, pp. 1151–56.
49. R.E. Logé, Y.B. Chastel, M.Y. Perrin, J.W. Signorelli, and R.A. Lebensohn: in Hot Extrusion of Zircaloy-4 Tubes: Induced Crystallographic Textures and Influence of the Initial Microstructure, Mathematical Modeling in Metal Processing and Manufacturing, P. Martin, W.J. Liu, S. MacEwen, Y. Verreman and J. Goldak, eds., The Metallurgical Society of CIM, Canada, 2000.
50. L. Whitmarsh: *Review of Zircaloy-2 and Zircaloy-4 Properties Relevant to NS Savannah Reactor Design, ORNL-3281*, Oak Ridge National Laboratory, Oak Ridge, 1962.
51. B.M. Pande and R.P. Agarwala: *J. Nucl. Mater.*, 1972, vol. 42, pp. 43–48.
52. B.M. Pande, M.C. Naik, and R.P. Agarwala: *J. Nucl. Mater.*, 1968, vol. 28, pp. 324–32.
53. C. Herzig and H. Eckseler: *Z. Metallkd.*, 1979, vol. 70, pp. 215–23.
54. ASM International Handbook Committee: *Metals Handbook. Vol. 1—Properties and Selection: Irons, Steels, and High-Performance Alloys*, 10th ed., ASM International, Metals Park, OH, 1990.
55. ASM International Handbook Committee: *Metals Handbook. Vol. 2—Properties and Selection: Nonferrous Alloys and Special-Purpose Materials*, 10th ed., ASM International, Metals Park, OH, 1990.
56. C. Evans: Micromechanisms and Micromechanics of Zircaloy-4, Doctoral Thesis Imperial College, London, UK, 2014.
57. J.H. Kim, M.H. Lee, B.K. Choi, and Y.H. Jeong: *J. Nucl. Sci. Technol.*, 2007, vol. 44, pp. 1275–80.
58. A. Macwan and D.L. Chen: *Mater. Des.*, 2015, vol. 84, pp. 261–69.
59. W. Xu, L. Liu, Y. Zhou, H. Mori, and D.L. Chen: *Mater. Sci. Eng. A*, 2013, vol. 563, pp. 125–32.
60. V.K. Patel, D.L. Chen, and S.D. Bhole: *Theor. Appl. Mech. Lett.*, 2014, vol. 4, pp. 041005-1–8.
61. S.H. Chowdhury, D.L. Chen, S.D. Bhole, X. Cao, and P. Wanjara: *Mater. Sci. Eng. A*, 2013, vol. 562, pp. 53–60.
62. A.D. Pelton, L. Leibowitz, and R.A. Blomquist: *J. Nucl. Mater.*, 1993, vol. 201, pp. 218–24.
63. K. Zeng, M. Hämäläinen, and R. Luoma: *Z. Metallkd.*, 1993, vol. 84, pp. 23–28.
64. J. Bodega, J.F. Fernández, F. Leardini, J.R. Ares, and C. Sánchez: *J. Phys. Chem. Solids*, 2011, vol. 72, pp. 1334–42.